

Strong ($H\beta$ + $[OIII]$) and $H\alpha$ emitters at redshift $z \simeq 7-8$ unveiled with JWST/NIRCam and MIRI imaging in the Hubble eXtreme Deep Field (XDF)

P. RINALDI,¹ K. I. CAPUTI,^{1,2} L. COSTANTIN,³ S. GILLMAN,^{2,4} E. IANI,¹ P. G. PÉREZ-GONZÁLEZ,³ G. ÖSTLIN,⁵
 L. COLINA,^{6,2} T. GREVE,^{2,4} H. U. NOORGARD-NIELSEN,^{2,4} G. S. WRIGHT,⁷ A. ALONSO-HERRERO,⁸
 J. ÁLVAREZ-MÁRQUEZ,⁶ A. ECKART,⁹ M. GARCÍA-MARÍN,¹⁰ J. HJORTH,¹¹ O. ILBERT,¹² S. KENDREW,¹⁰ A. LABIANO,¹³
 O. LE FÈVRE,¹² J. PYE,¹⁴ T. TIKKANEN,¹⁴ F. WALTER,¹⁵ P. VAN DER WERF,¹⁶ M. WARD,¹⁷ M. ANNUNZIATELLA,^{3,18}
 A. BIK,¹⁹ L. BOOGARD,¹⁵ S. BOSMAN,¹⁵ A. CRESPO,⁶ I. JERMANN,^{2,4} D. LANGEROODI,¹¹ J. MELINDER,⁵ R. MEYER,¹⁵
 T. MOUTARD,¹² F. PEISSKER,⁹ M. TOPINKA,²⁰ E. VAN DISHOCK,¹⁶ M. GÜDEL,^{21,22,23} TH. HENNING,¹⁵ P.-O. LAGAGE,²⁴
 T. RAY,²⁰ B. VANDENBUSSCHE,²⁵ AND C. WAELENS²⁵

¹*Kapteyn Astronomical Institute, University of Groningen, P.O. Box 800, 9700AV Groningen, The Netherlands*

²*Cosmic Dawn Center (DAWN), Denmark*

³*Centro de Astrobiología, (CAB, CSIC-INTA), Carretera de Ajalvir km 4, E-28850 Torrejn de Ardoz, Madrid, Spain*

⁴*DTU-Space, Elektrovej, Building 328, 2800, Kgs. Lyngby, Denmark*

⁵*Department of Astronomy, Stockholm University, Oscar Klein Centre, AlbaNova University Centre, 106 91 Stockholm, Sweden*

⁶*Centro de Astrobiología, (CAB, CSIC-INTA), Carretera de Ajalvir km 4, E-28850 Torrejón de Ardoz, Madrid, Spain*

⁷*UK Astronomy Technology Centre, Royal Observatory Edinburgh, Blackford Hill, Edinburgh EH9 3HJ, UK*

⁸*Centro de Astrobiología (CAB), CSIC-INTA, Camino Bajo del Castillo s/n, E-28692 Villanueva de la Cañada, Madrid, Spain*

⁹*I. Physikalisches Institut der Universität zu Köln, Zùlpicher Str. 77, 50937 Köln, Germany*

¹⁰*European Space Agency/Space Telescope Science Institute, 3700 San Martin Drive, Baltimore MD 21218, USA*

¹¹*DARK, Niels Bohr Institute, University of Copenhagen, Jagtvej 128, 2200 Copenhagen, Denmark*

¹²*Aix Marseille Université, CNRS, LAM (Laboratoire d'Astrophysique de Marseille) UMR 7326, 13388, Marseille, France*

¹³*Telespazio UK for the European Space Agency (ESA), ESAC, Camino Bajo del Castillo s/n, 28692 Villanueva de la Cañada, Spain.*

¹⁴*School of Physics & Astronomy, Space Research Centre, Space Park Leicester, University of Leicester, 92 Corporation Road, Leicester, LE4 5SP, UK*

¹⁵*Max-Planck-Institut für Astronomie, Königstuhl 17, 69117 Heidelberg, Germany*

¹⁶*Leiden Observatory, Leiden University, PO Box 9513, 2300 RA Leiden, The Netherlands*

¹⁷*Centre for Extragalactic Astronomy, Durham University, South Road, Durham DH1 3LE, UK*

¹⁸*INAF-Osservatorio Astronomico di Capodimonte, Via Moirariello 16, I-80131 Napoli, Italy*

¹⁹*Department of Astronomy, Stockholm University, Oscar Klein Centre, AlbaNova University Centre, 106 91 Stockholm, Sweden*

²⁰*Dublin Institute for Advanced Studies, 31 Fitzwilliam Place, D02 XF86 Dublin, Ireland*

²¹*Dept. of Astrophysics, University of Vienna, Trkenschanzstr 17, A-1180 Vienna, Austria*

²²*Max-Planck-Institut für Astronomie (MPIA), Königstuhl 17, 69117 Heidelberg, Germany*

²³*ETH Zurich, Institute for Particle Physics and Astrophysics, Wolfgang-Pauli-Str. 27, 8093 Zurich, Switzerland*

²⁴*AIM, CEA, CNRS, Université Paris-Saclay, Université Paris Diderot, Sorbonne Paris Cité, F-91191 Gif-sur-Yvette, France*

²⁵*Institute of Astronomy, KU Leuven, Celestijnenlaan 200D bus 2401, 3001 Leuven, Belgium*

Submitted to ApJ

ABSTRACT

The *JWST* is revolutionizing the study of high-redshift galaxies by providing for the first time a high-sensitivity view of the early Universe at infrared wavelengths, both with its Near Infrared Camera (NIRCam) and Mid Infrared Instrument (MIRI). In this paper we make use of medium and broadband NIRCam imaging, as well as ultra-deep MIRI 5.6 μ m imaging, in the Hubble eXtreme Deep Field (XDF) to identify prominent line emitters at $z \simeq 7-8$. Out of a total of 58 galaxies at $z \simeq 7-8$, we find 18 robust candidates ($\simeq 31\%$) for prominent ($H\beta$ + $[OIII]$) emitters, based on their enhanced fluxes in

the F430M and F444W filters, with rest-frame $\text{EW}(\text{H}\beta + [\text{OIII}]) \simeq 87 - 2100 \text{ \AA}$. Among these emitters, 16 lie on the MIRI coverage area and 12 show a clear flux excess at $5.6 \mu\text{m}$, indicating the simultaneous presence of a prominent $\text{H}\alpha$ emission line with rest-frame $\text{EW}(\text{H}\alpha) \simeq 200 - 3000 \text{ \AA}$. This is the first time that $\text{H}\alpha$ emission can be detected in individual galaxies at $z > 7$. The $\text{H}\alpha$ line, when present, allows us to separate the contributions of the $\text{H}\beta$ and $[\text{OIII}]$ emission lines to the $(\text{H}\beta + [\text{OIII}])$ complex and derive $\text{H}\alpha$ -based star formation rates (SFRs). We find that in some cases $[\text{OIII}]/\text{H}\beta > 1$, suggesting low metallicities, but a few have $[\text{OIII}]/\text{H}\beta < 1$, so the NIRCcam flux excess is mainly driven by $\text{H}\beta$. The vast majority of prominent line emitters are very young starbursts or galaxies on their way to/from the starburst cloud. They make for a cosmic SFR density $\log_{10}(\rho_{\text{SFR}_{\text{H}\alpha}}/\text{M}_{\odot} \text{ yr}^{-1} \text{ Mpc}^{-3}) \simeq -2.35$, which is about a third of the total value at $z \simeq 7 - 8$. Therefore, the strong $\text{H}\alpha$ emitters likely had an important role in reionization.

Keywords: Galaxies: formation, evolution, high-redshift, star formation, starburst, Epoch of Reionization

1. INTRODUCTION

Quantifying the presence and properties of galaxies present at the Epoch of Reionization (EoR) is necessary to explain how this major phase transition of the Universe has occurred. Over the past decade many studies have focused on this topic, but a few important problems complicated the selection of galaxies at this cosmic time. The increasing intergalactic medium absorption with redshift means that basically all photons blueward of the Lyman- α spectral line at $\lambda_{\text{rest}} = 1216 \text{ \AA}$ cannot reach us. Indeed, it is well known that the incidence of Lyman- α emitters (LAEs) has a sharp drop at $z > 7$ (e.g., Fontana et al. 2010; Ono et al. 2012; Caruana et al. 2014; Pentericci et al. 2014). Therefore, other emission lines at longer wavelengths must be considered to facilitate the search of galaxies at such high redshifts (e.g., Stark et al. 2015).

However, detecting the optical emission from atomic transitions at $z > 7$ was virtually impossible until now, given the lack of sufficiently sensitive near and mid-infrared observatories. The recent advent of the *JWST* is now radically changing this situation by offering, for the first time, sensitive imaging and spectroscopy at such long wavelengths. Indeed, in the first six months of operations, *JWST* has enabled a number of studies of $z > 7$ galaxies, particularly on their line emission properties (e.g., Arellano-Córdova et al. 2022; Morishita & Stiavelli 2022; Trump et al. 2022; Wang et al. 2022).

With imaging, the search of line emitters is facilitated by the fact that the rest-frame equivalent widths (EW) of some of the main optical emission lines appears to increase, on average, with redshift (e.g., De Barros et al. 2019; Matthee et al. 2022). This has allowed for the search of prominent line emitters at intermediate and high redshifts, by identifying galaxies with photometric excess in narrow-band images (e.g., Khostovan et al. 2016) and even broad-band images (e.g., Faisst et al.

2016; Roberts-Borsani et al. 2016; Smit et al. 2016; Caputi et al. 2017). This trend of increasing rest-frame EWs with redshift is indicative of an evolution in the galaxy average specific star formation rates (sSFR) (e.g., Faisst et al. 2016; Tang et al. 2019), as well as the conditions of their interstellar medium (ISM, Schaerer & de Barros 2009).

At $z > 7$ both the $\text{H}\beta \lambda 4861 \text{ \AA}$ and $[\text{OIII}] \lambda\lambda 4959, 5007$ emission lines are shifted into the *JWST*'s Near-IR Camera (NIRCcam; Rieke et al. 2005) wavelength range, making that these lines together can produce a flux excess in the NIRCcam filters at $\simeq 4 - 5 \mu\text{m}$. In turn, the $(\text{H}\alpha \lambda 6563 + [\text{NII}] \lambda\lambda 6548, 6583 + [\text{SII}] \lambda\lambda 6716, 6730)$ complex appears in the Mid-Infrared Instrument (MIRI; Rieke et al. 2015; Wright et al. 2015) wavelength domain at observed $> 5 \mu\text{m}$.

In this paper we make use of publicly available NIRCcam images in the Hubble eXtreme Deep Field (XDF) to search for $(\text{H}\beta + [\text{OIII}])$ emitters at $z \simeq 7 - 8$. In most of this field, we also benefit from ultra-deep MIRI $5.6 \mu\text{m}$ imaging, which we analyse to search for the presence of $\text{H}\alpha$ emission in the same galaxies. This is the first time that the $\text{H}\alpha$ line can be detected and quantified in individual galaxies at $z > 7$. This paper is organised as follows: in §2 we describe the datasets, photometric measurements and spectral energy distribution (SED) fitting that allows us to select galaxies at $z \simeq 7 - 8$. In §3 we explain our methodology to identify strong $(\text{H}\beta + [\text{OIII}])$ and $\text{H}\alpha$ emitters amongst these galaxies. We present all our results in §4 and our conclusions in §5. Throughout this paper, we consider a cosmology with $H_0 = 70 \text{ km s}^{-1} \text{ Mpc}^{-1}$, $\Omega_{\text{M}} = 0.3$ and $\Omega_{\Lambda} = 0.7$. All magnitudes are total and refer to the AB system (Oke & Gunn 1983). A Chabrier (2003) initial mass function (IMF) is assumed.

2. DATASETS, PHOTOMETRY AND SED FITTING

2.1. Datasets

The Hubble XDF (Illingworth et al. 2013, see Fig. 1) is a small field of the sky with the deepest *Hubble Space Telescope* (*HST*) observations ever taken since this telescope started operations more than thirty years ago. This field has been the main window to study the early Universe before the *JWST* advent, with numerous works scientifically exploiting its unique possibilities. Now in the *JWST* era, the *HST* data in the XDF and surroundings are being enhanced with deep imaging and spectroscopy obtained with *JWST*/NIRCam and MIRI, extending the wavelength coverage of high spatial-resolution observations to the mid-infrared.

2.1.1. *JWST*/NIRCam

In this work we made use of the recent *JWST*/NIRCam images collected by Williams et al. (2021) in a General Observers Cycle-1 program across the HUDF (PID: 1963; PI: Christina C. Williams). Observations have been taken in 5 *JWST*/NIRCam medium bands: F182M, F210M, F430M, F460M, and F480M. In particular, 7.8 hours of the total integration time have been dedicated to F182M, F210M, and F480M. Instead, only 3.8 hours of observations have been collected for F430M and F460M. In order to complement these datasets, we also made use of the imaging data taken as part of *The First Reionization Epoch Spectroscopic COmplete Survey* (Oesch et al. 2021, FRESCO) (PID: 1895; PI: Pascal Oesch). On the one hand, this GO program allowed us to add more depth to F182M and F210M, on the other hand it gave us the opportunity to include F444W in our analysis.

All the *JWST*/NIRCam images have been reduced utilising a modified version of the official *JWST* pipeline¹. The reduction we adopted in this paper is based on `jwst` version 1.8.2 and Calibration Reference Data System pipeline mapping (CRDS; pmap) 1018. More detailed information about those reference files are available on the official STScI/CRDS website.

Compared to the official *JWST* pipeline, our version includes different procedures, following some of the ideas presented in Bagley et al. (2022), to deal with the unresolved problems that still affect the official software. In our data reduction, we minimized the impact of the so-called snowballs, the $1/f$ noise, the wisps², and the residual cosmic rays. After reducing all the

JWST/NIRCam images from Williams’s and FRESCO programs, we drizzled all the NIRCam calibrated files to 0.03 arcsec/pixel, as the final pixel scale we adopted in this work. All the final images have been aligned to the Hubble Legacy Fields (HFL) catalogue³.

As a sanity check, we compared the photometry for the brightest sources (< 24 mag) in all the NIRCam filters. To do that, we produced two versions of our final images, with and without the extra steps we employed in our modified version of the official pipeline. Then, we extracted the sources by using the software **Source Extractor** (SExtractor, Bertin & Arnouts 1996) and compared their photometry. This test demonstrated that our extra steps do not introduce any kind of systematic effect in the photometry.

2.1.2. *JWST*/MIRI

We complemented the *JWST*/NIRCam observations with the MIRI 5.6 μ m imaging from the *JWST* Guaranteed Time Observations (GTO) program *The MIRI HUDF Deep Imaging Survey* (PID: 1283, PI: Göran Östlin). The MIRI observations were carried out in December 2022 and targeted with the broad-band filter F560W the HUDF for a total amount of 50 hours, covering an area of about 4.7 arcmin². By reaching a median depth of 29.15 mag (5σ , $r = 0.15$ arcsec), this set of observations represents the deepest imaging available at 5.6 μ m to date. A complete description of the data collection and reduction, as well as the source statistics on these 5.6 μ m images, will be presented by Ostlin et al. (2023, in prep.). Here we only summarize the basic information of these data processing.

As in the case of the NIRCam imaging, we adopted a modified version of the official *JWST* pipeline to reduce the MIRI data. In fact, the final products that can be obtained by running the *JWST* pipeline are still affected by strong patterns (e.g. vertical striping, background gradients) that impact the scientific quality of the images (e.g. Iani et al. 2022). To overcome these problems, we added to the pipeline some extra steps at the end of stages 2 and 3 that allowed us to significantly mitigate the intensity of the striping, the background inhomogeneities as well as the noise of the output image. A comparison between the F560W magnitude of the brightest galaxies (< 24 mag) measured in MIRI images obtained with and without the extra steps ensured that our modified version of the pipeline did not introduce any systematic offset.

¹ The pipeline is available at <https://github.com/spacetelescope/jwst>

² More information about these artefacts here: <https://jwst-docs.stsci.edu/jwst-near-infrared-camera/nircam-features-and-caveats/nircam-claws-and-wisps>

³ The catalogue is available here: <https://archive.stsci.edu/hlsps/hlf/>

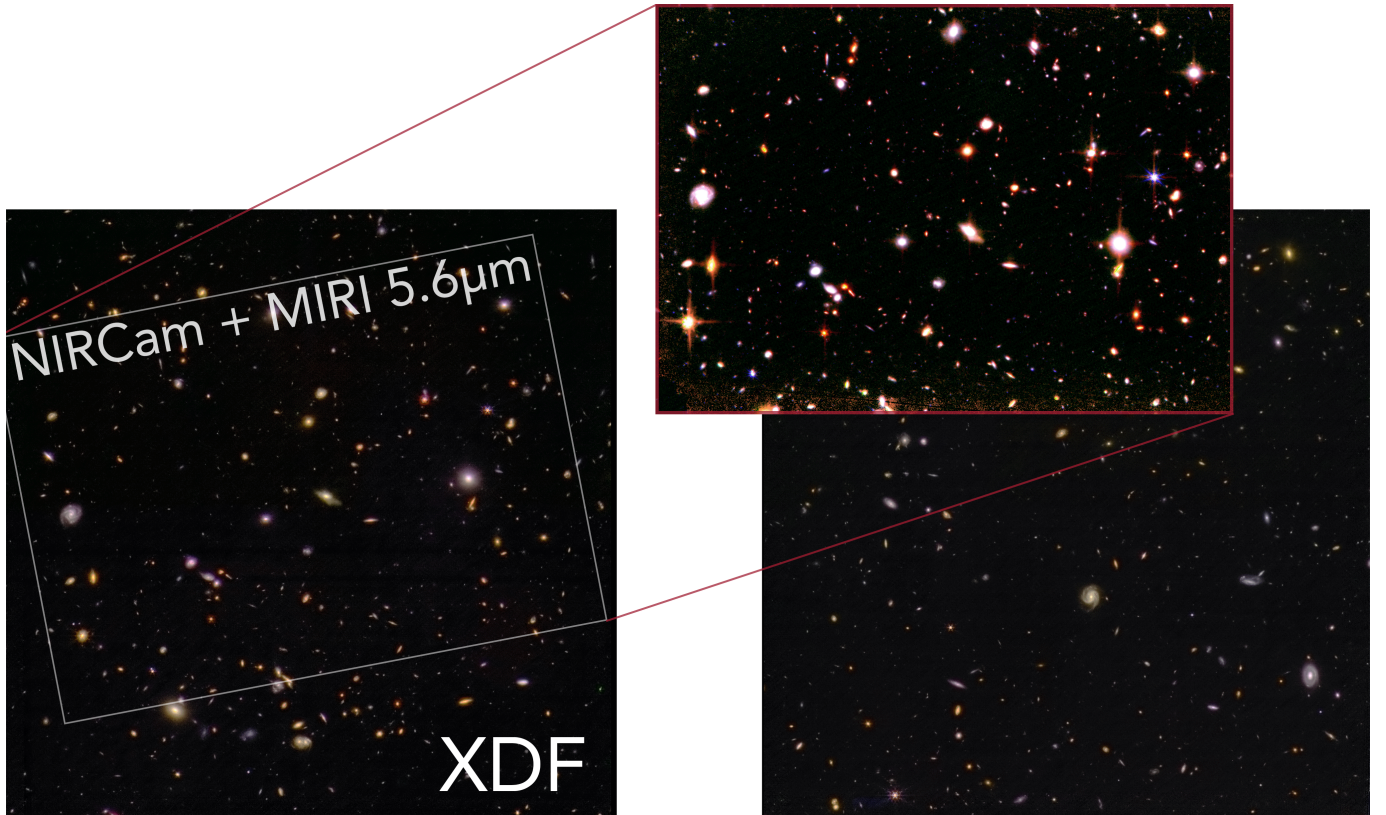


Figure 1. An RGB mosaic of the Hubble eXtreme Ultra Deep Field. This image has been obtained by exploiting the *HST* and *JWST* images currently available in this field. In particular, the background image has been obtained by combining *HST* and *JWST*/NIRCam filters. The zoom-in shows the region covered by MIRI/F560W. In this case, to create the RGB image, we adopted the *JWST* filters only where R: F560W; G: F430M, F444W, F460M, and F480M; B: F182M and F210M. The RGB images have been produced using the software PixInsight. Credits to: Rafael Navarro-Carrera/NASA/ESA.

Finally, we drizzled the final MIRI image to the same pixel scale adopted for the *JWST*/NIRCam images and registered its astrometry to the HLF catalogue.

2.1.3. Ancillary *HST* data

We obtained all of *HST* images over the HUDF from the Hubble Legacy Field GOODS-S (HLF-GOODS-S)⁴. The HLF-GOODS-S provides 13 *HST* bands covering a wide range of wavelengths ($0.2\mu\text{m}$ - $1.6\mu\text{m}$), from the UV (WFC3/UVIS F225W, F275W, and F336W filters), optical (ACS/WFC F435W, F606W, F775W, F814W and F850LP filters), to near-infrared (WFC3/IR F098M, F105W, F125W, F140W and F160W filters). See Whitaker et al. (2019) for more detailed information on these observations.

2.2. Photometric Analysis

We used the software SExtractor to detect the sources and measure their photometry in all the 20 filters

available from *HST* and *JWST*, covering a wide range of wavelengths ($0.2\mu\text{m}$ - $5.6\mu\text{m}$). We used SExtractor in dual-image mode adopting a super-detection image that we created by combining photometric information from different bands. In order to maximize the number of the detected sources, we opted to use a *hot-mode* extraction, as presented in Galametz et al. (2013) which is well suited to find very faint sources.

We combined aperture photometry, adopting circular apertures (i.e., MAG_APER) of $0.5''$ diameter, and Kron apertures (i.e., MAG_AUTO, Kron 1980) following the same prescription we adopted in Rinaldi et al. (2022, see section 3.2). We chose a circular-aperture flux over a Kron flux when the sources were fainter than a given magnitude. In this case, since we were dealing with very deep images, we decided to consider $\text{mag} = 27$ as our upper limit for the Kron aperture. This final decision has been taken after several tests we performed with the *HST* photometry, comparing our fluxes with the HLF photometric catalogue from Whitaker et al. (2019). We corrected the aperture fluxes to total. For *HST*, these

⁴ The *HST* images ($0.03 \text{ arcsec/pixel}$) have been downloaded from <https://archive.stsci.edu/prepds/hlf/>

corrections are well known⁵⁶⁷. For *JWST*, instead, we estimated the aperture corrections using the **WebbPSF**⁸ software.

Moreover, we adopted a minimum error of 0.05 mag for all the HST photometry because **SExtractor** typically underestimates photometric errors (e.g., [Sonnett et al. 2013](#)). We decided to adopt this minimum error value for the *JWST* images as well to account for possible uncertainties in the NIRC*am* and MIRI flux calibrations.

Finally, all our fluxes have been corrected for Galactic extinction. Those values have been estimated adopting a python package called **dustmap**⁹. As a sanity check, we compared the correction factors for the *HST* filters with [Schlafly & Finkbeiner \(2011\)](#), finding an excellent agreement with the values we can recover following their prescription, as expected.

2.3. SED fitting

We performed the SED fitting and derived the properties of our sources making use of the code **LePHARE** ([Arnouts & Ilbert 2011](#)). We constructed the libraries for **LePHARE** adopting the same configuration for the star formation histories (SFHs) we used in [Rinaldi et al. \(2022, see section 4\)](#). To build our libraries, we considered the stellar population synthesis (SPS) models proposed by [Bruzual & Charlot \(2003, hereafter BC03\)](#), based on the Chabrier IMF ([Chabrier 2003](#)). In particular, we adopted two and distinct metallicity values, a solar metallicity ($Z_{\odot} = 0.02$) and a fifth of solar metallicity ($Z = 0.2Z_{\odot} = 0.004$). Moreover, to take into account the strong contribution from the nebular emission lines that can occur at very young ages, we also considered **STARBURST99** templates ([Leitherer et al. 1999, hereafter SB99](#)) for young galaxies (age $\leq 10^7$ yr) with constant star formation histories. We considered the [Calzetti et al. \(2000\)](#) reddening law with color excess values $0 \leq E(B - V) \leq 1.5$, with a step of 0.1.

We estimated upper limits for each source that **SExtractor** was not able to detect. To do that, around each source, we placed random circular apertures (0.5'' arcsec diameter) to estimate the background r.m.s. (1σ).

For **LePHARE**, we opted to use the 3σ upper limit for the flux in those filters where we did not have a detection. Finally, we adopted -99 for those filters where we did not have any photometric information (e.g., the MIRI/F560W and NIRC*am* coverage areas are different).

3. SELECTION OF STRONG ($H\beta$ + $[OIII]$) AND $H\alpha$ EMITTERS AT $z \simeq 7 - 8$

LePHARE returns the best-fit SED and derived parameters for each source. We performed two different runs with **LePHARE**, one adopting BC03 models only and the other one adopting SB99 models only. Therefore, we created the final catalogue choosing for each source the best χ^2_{ν} between the BC03 and SB99 solutions. Finally, we cleaned our catalogue from possible stars. To do so, we first cross-matched our catalogue with *Gaia* Data Release 3 ([Babusiaux et al. 2022](#)). Then, we looked at the stellarity parameter (i.e., **CLASS_STAR**) we have from **SExtractor**. In particular, we applied the same criterion adopted in [Caputi et al. \(2011, Section 3.1\)](#). We removed all those sources that have **CLASS_STAR** > 0.8 and occupy the stellar locus in the (F435W - F125W) versus (F125W - F444W) colour-colour diagram.

Since our goal is to look for potential ($H\beta + [OIII]$) and ($H\alpha + [NII] + [SII]$) emitters in the XDF at $z \simeq 7 - 8$, we only focused on those sources for which the best photometric redshift falls in that redshift range.

For each candidate, we created postage stamps to make a careful visual inspection in order to exclude all those galaxies that either fall on stellar spikes or are heavily contaminated by the light of the nearby sources. After this visual inspection, we were left with 58 robust galaxy candidates at $z \simeq 7 - 8$.

Among these sources, we searched for ($H\beta + [OIII]$) and $H\alpha$ emitters. We first analysed if they show a flux excess in the following three bands: NIRC*am*/F430M, NIRC*am*/F444W, and MIRI/F560W. The first two filters have been used to look at the flux enhancement produced by ($H\beta + [OIII]$). In turn, MIRI/F560W has been used to look at the flux excess produced by $H\alpha$. To convert the flux excess into a rest-frame EW we followed the procedure described by [Mármol-Queraltó et al. \(2016\)](#).

To estimate the flux excess, we assumed that the continuum flux was well described by the synthetic NIRC*am*/F460M obtained from the best-fit template for each galaxy. In particular, we selected all those sources for which $|\text{mag}_{\text{obs}}(\text{F460M}) - \text{mag}_{\text{syn}}(\text{F460M})| \leq 2 \times \text{mag}_{\text{err}}(\text{F460M})$, where mag_{obs} and mag_{syn} are the observed and best-fit synthetic magnitudes, respectively. This condition ensures that the continuum at $4.6\mu\text{m}$ can be considered flat within the error bars. We also

⁵ ACS: <https://www.stsci.edu/hst/instrumentation/acs/data-analysis/aperture-corrections>

⁶ WFC/IR: <https://www.stsci.edu/hst/instrumentation/wfc3/data-analysis/photometric-calibration/ir-encircled-energy>

⁷ WFC3/UVIS: <https://www.stsci.edu/hst/instrumentation/wfc3/data-analysis/photometric-calibration/uvis-encircled-energy>

⁸ **WebbPSF** is available at <https://webbpsf.readthedocs.io/en/latest/>

⁹ This python package is available at <https://github.com/gregreen/dustmaps/blob/master/docs/index.rst>

double-checked if this condition was satisfied in NIRCam/F480M.

Once we selected all those sources that survive the condition described above, we estimated the flux excess in the following way: $\Delta\text{mag} = (\text{mag}_X - \text{mag}_{\text{cont}})$, where mag_X represents the magnitude in one of the filters we chose to select ($\text{H}\beta + [\text{OIII}]$) or $\text{H}\alpha$, and mag_{cont} refers to $\text{F460M}_{\text{syn}}$. For a conservative approach, we only considered those galaxies for which the flux excess with respect to the stellar continuum satisfies the following condition: $\Delta\text{mag} < -0.2$. Note that a $\Delta\text{mag} = -0.2$ in NIRCam/F430M corresponds to a rest-frame EW $\simeq 58 \text{ \AA}$ at $z = 7$, while in NIRCam/F444W it would imply a rest-frame EW $\simeq 270 \text{ \AA}$. For MIRI/F560W, the same Δmag would correspond to a rest-frame EW $\simeq 239 \text{ \AA}$ at the same redshift.

We inspected again the postage stamps of the 58 possible candidates, after estimating the flux excess in each band (NIRCam/F430M, NIRCam/F444W, and MIRI/F560W), to make a cross-match between the values we got for Δmag and the visual inspection of the sources themselves. We also examined the best-fit SED for each galaxy. This safely allowed us to conclude that 18 sources can be securely classified as ($\text{H}\beta + [\text{OIII}]$) emitters. These emitters constitute $\simeq 31\%$ of our total galaxy sample at $z \simeq 7 - 8$ (see Fig. 2 where we show the multiwavelength images of an example source). The derived rest-frame EW values cover a wide range that goes from a minimum of 87.51 \AA to a maximum value of 2140.41 \AA , with a median rest-frame $\langle \text{EW} \rangle \simeq 943^{+737}_{-194} \text{ \AA}$. This value is higher, but still marginally consistent within the error bars, than that derived by Labbé et al. (2013) from *Spitzer Space Telescope* observations of bright $z \simeq 8$ galaxy candidates. Out of the 18 ($\text{H}\beta + [\text{OIII}]$) emitters, 83% of them have a best-fit SED with sub-solar ($0.2 Z_{\odot}$) metallicity and the remaining $\sim 17\%$ with solar (Z_{\odot}) metallicity.

Among the 18 ($\text{H}\beta + [\text{OIII}]$) emitters at $z \simeq 7 - 8$, a total of 16 lie on the ultra-deep MIRI $5.6 \mu\text{m}$ coverage field. Out of them, 12 show a significant $5.6 \mu\text{m}$ flux excess with respect to the continuum (as defined above), which we interpret as the presence of the ($\text{H}\alpha + [\text{NII}] + [\text{SII}]$) line complex at $z \simeq 7 - 8$. To obtain the net value of the $\text{H}\alpha$ rest EW, we applied the correction recipes provided by Anders & Fritze-v. Alvensleben (2003), as follows: $f(\text{H}\alpha) = 0.63f(\text{H}\alpha + [\text{NII}] + [\text{SII}])$ for a solar metallicity, and $f(\text{H}\alpha) = 0.81f(\text{H}\alpha + [\text{NII}] + [\text{SII}])$ for a $0.2 Z_{\odot}$ metallicity. Note that with this procedure we are assuming that the stellar and gas metallicities are similar in these galaxies.

4. RESULTS

Once we estimated the stellar properties of our candidates by performing the SED fitting with LePHARE, we analysed the properties of these sources by comparing our results with the recent literature at high redshifts. Before doing that, we first ensured that the stellar masses we inferred with LePHARE were not affected by the presence of the flux excess we estimated in F430M, F444W, and F560W. To do that, we re-run LePhare following the same methodology explained by Caputi et al. (2017). This time, for each source, we turned off those bands (NIRCam/F430M, NIRCam/F444W, and MIRI/F560W) in which we found a flux excess (i.e., -99 following LePHARE's prescription). Moreover, for this run, we fixed the redshifts adopting the photometric ones we estimated from the original run. Doing this test allows us to ensure that our stellar mass estimates are not affected by any emission line that falls in one of those filters. We found a good agreement within 2σ . Finally, we also inspected that the stellar continuum was well-described by inspecting the best-fit SEDs we obtained from LePHARE. In Fig. 3 we show two examples (ID: 9432, 9434) of the best-fit SEDs for the candidates we have in our sample.

4.1. Emission line EW versus Stellar Mass and Age in galaxies at $z \simeq 7 - 8$

Having calculated the ($\text{H}\beta + [\text{OIII}]$) rest-frame EW for the prominent line emitters, we can compare their best-fit SED properties with those of the other $z \simeq 7 - 8$ galaxies in our sample. In Fig. 4, we show the derived ($\text{H}\beta + [\text{OIII}]$) rest-frame EW versus best-fit age. From this plot, we can see that all except three of the ($\text{H}\beta + [\text{OIII}]$) emitters are characterised by very young best-fit ages ($< 10^{7.5} \text{ yr}$), which indicates that these objects may be in their first major star-formation episode. The remaining three objects are older ($> 10^8 \text{ yr}$), with two having almost the age of the Universe at their redshifts. This fact suggests that these galaxies could be having a rejuvenation episode, as those known to happen at lower redshifts (Rosani et al. 2020), as it is unlikely that they could have sustained their high instantaneous SFR values for all of their lifetimes.

The grey triangles in Fig. 4 refer to the EW upper limits that we estimated for all those galaxies at $z \simeq 7 - 8$ that do not have a significant flux excess in the NIRCam/F430M band. In contrast to the ($\text{H}\beta + [\text{OIII}]$) emitters, the non-emitters span different possible ages at those redshifts, without any bias towards young/old ages.

We also compared our results with the recent literature. In particular, Endsley et al. (2021) studied a sample of 20 rest-frame UV bright ($\text{H}\beta + [\text{OIII}]$) emitters at

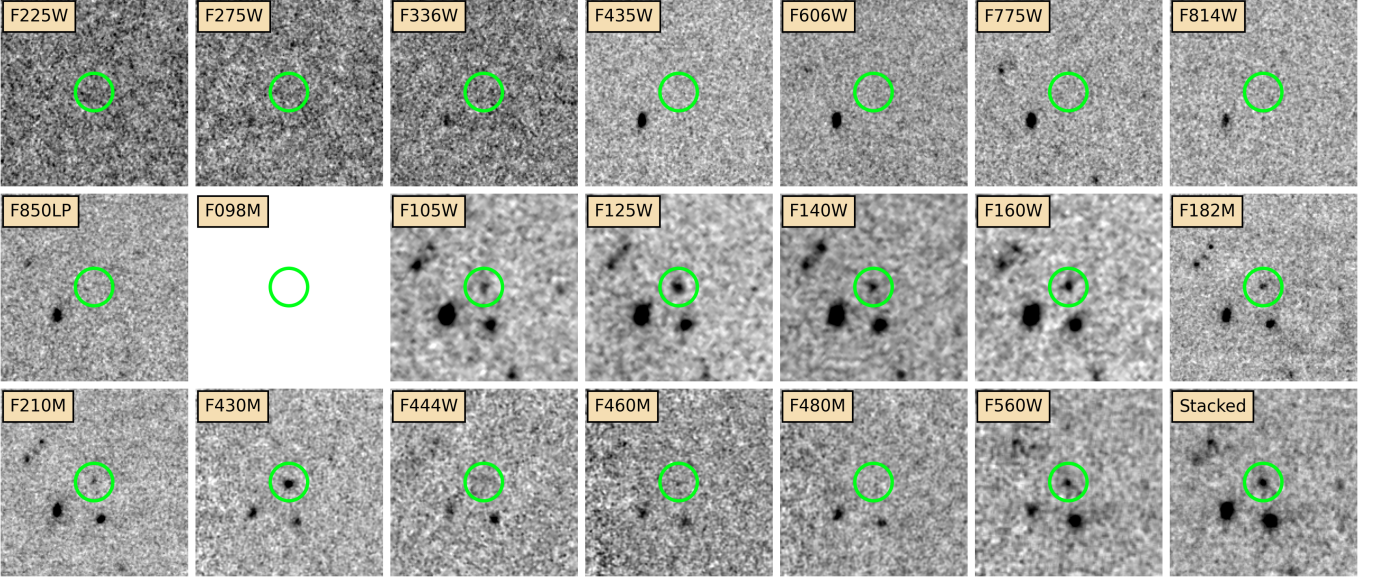


Figure 2. Postage stamps ($5'' \times 5''$) of one of our ($H\beta + [OIII]$) candidates (ID: 9434, $z_{best} = 7.68^{+0.03}_{-0.01}$). The last postage stamp refers to the stacked image we adopted as the detection map with **SExtractor**. Here we show all the bands we used in our analysis, from $0.2\mu m$ to $5.6\mu m$. The green circle has been placed to only guide the eye on the source. In particular, from these postage stamps, there is a clear excess at $4.3\mu m$. This source shows an excess in MIRI/F560W as well.

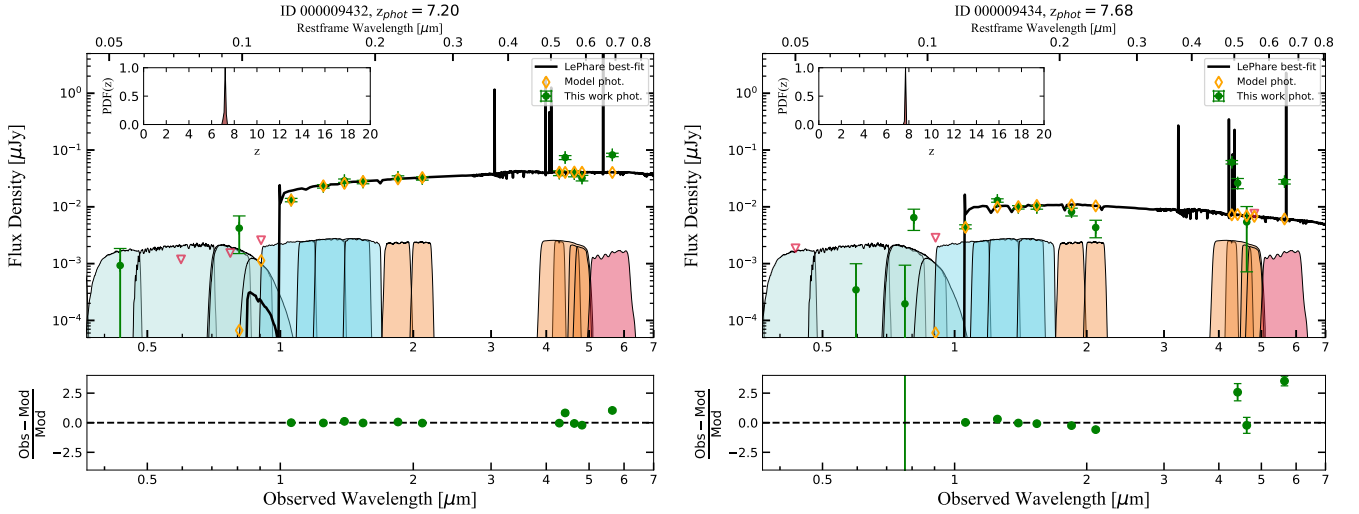


Figure 3. The best-fit SEDs for two examples of line-emitter candidates at $z \simeq 7 - 8$. On the left panel, we show a source at $z_{phot} \simeq 7.19$ (ID = 9432). On the right panel, we show another source at $z_{phot} \simeq 7.68$ (ID = 9434). Both panels show how well-constrained the best-fit SEDs and the derived photometric redshifts are, which is evident by simple inspection of the best-fit templates and their probability density functions (PDF(z)). In each case, we notice the clear presence of an excess in F430M, F444W, and F560W, which we adopted as the criterion to select our sample of ($H\beta + [OIII]$) and $H\alpha$ emitters.

$z \simeq 6.8 - 7$ that have been selected over a wide sky area (2.7 deg^2 in total). [Endsley et al. \(2021\)](#) found this rare population of very strong ($H\beta + [OIII]$) emitters with a rest-frame EW $> 1200 \text{ \AA}$. The fact that we find similarly high ($H\beta + [OIII]$) rest-frame EWs among faint galaxies in a much smaller area of the sky indicates that prominent ($H\beta + [OIII]$) emitters must have been quite common at the EoR.

Finally, the solid and dashed lines in Fig. 4 show the expected variation of the $H\beta$ (only) rest-frame EW versus age for **STARBURST99** model galaxies. These theoretical tracks are based on a Chabrier IMF with a stellar mass cut-off of $100M_{\odot}$ and were obtained both for a solar and a subsolar metallicity ($0.2Z_{\odot}$), each for a single burst and constant SFH. As expected, our data points are located nicely above these curves, following

the trend of the models with constant star formation histories, albeit with higher rest-frame EW, due to the [OIII] contribution.

Over the past decades, the recombination line equivalent widths have been used as proxies for stellar population age in star-forming galaxies. The ratios between the fluxes of the recombination line, which are sensitive to the instantaneous star-formation rates, and the fluxes of the continuum, which are sensitive to the previous average SFR, are indeed what we define as recombination line equivalent widths (Stasińska & Leitherer 1996). In particular, Reddy et al. (2018) found a very strong anti-correlation between $(H\beta + [OIII])$ rest-frame EW and young ages at $z \simeq 1.8 - 3.8$, which does not evolve as a function of redshift at that range of cosmic time. By looking at Fig. 4, we can see that this anti-correlation is evident also at $z \simeq 7 - 8$ where strong $(H\beta + [OIII])$ emitters prefer young ages, which is in line with what has been found at lower redshifts.

We repeated the same exercise looking, this time, at the derived $(H\beta + [OIII])$ rest-frame EW versus stellar mass for our $(H\beta + [OIII])$ emitters (Fig. 5). Also in this case, the stellar masses come directly from the best-fit SED obtained with LePHARE. As we can see from Fig. 5, our $(H\beta + [OIII])$ emitters have a stellar mass that ranges from a minimum value of $\log_{10}(M_*/M_\odot) \simeq 7.5$ to a maximum value of $\log_{10}(M_*/M_\odot) \simeq 9$. In previous works it has been shown that the normalization of the $(H\beta + [OIII])$ rest-frame EW versus stellar mass relation should increase with redshift (e.g., Reddy et al. 2018). Here we find a broad anti-correlation between the two quantities. The grey triangles in Fig. 5 refer to the upper limits that we estimated for the $(H\beta + [OIII])$ rest-frame EW for the $z \simeq 7 - 8$ galaxies that are not classified as emitters from a NIRCam flux excess.

Finally, for all those galaxies that show an “ $H\alpha$ excess”, we compare their $(H\beta + [OIII])$ rest-frame EW versus $(H\alpha + [NII] + [SII])$ rest-frame EW. We show this comparison in Fig. 6. We see that our sample does not follow any correlation between these two EWs, which also suggests that the $(H\beta + [OIII])$ complex contains a variety of [OIII] contributions. As a matter of fact, as we can derive the $H\alpha$ line flux from our data, we can also infer the $H\beta$ line flux independently and separate the contributions of $H\beta$ and [OIII] for each galaxy, considering the following:

$$f(H\beta) = f(H\alpha) \times 10^{-0.4 \times 1.27E(B-V)} / 2.86, \quad (1)$$

where $f(H\alpha)$ and $f(H\beta)$ refer to the observed fluxes and $E(B - V)$ is the colour excess obtained from the best-fit SED model. The denominator 2.86 corresponds

to assuming case B recombination (e.g. Osterbrock & Ferland 2006), while the factor $-1.27 = k(H\alpha) - k(H\beta)$ is obtained from the Calzetti et al. (2000) reddening law.

Once we know the $H\beta$ flux for each source, we can independently work out the [OIII] $\lambda\lambda 4959, 5007$ fluxes for all those emitters that show an $H\alpha$ excess.

The data points in Fig. 6 are colour-coded according to each galaxy’s [OIII] $\lambda 5007/H\beta$ ratio. From that figure, we clearly see that the few emitters whose ratio is dominated by $H\beta$ (i.e., $[OIII]/H\beta < 1$) are placed well above the identity line. These sources show an $H\alpha$ rest-frame EW greater than that one inferred for the $(H\beta + [OIII])$ complex. There are a few other galaxies which also lie above the identity line, but with $[OIII]/H\beta > 1$. This can be explained by the non-negligible dust extinction affecting these galaxies SEDs.

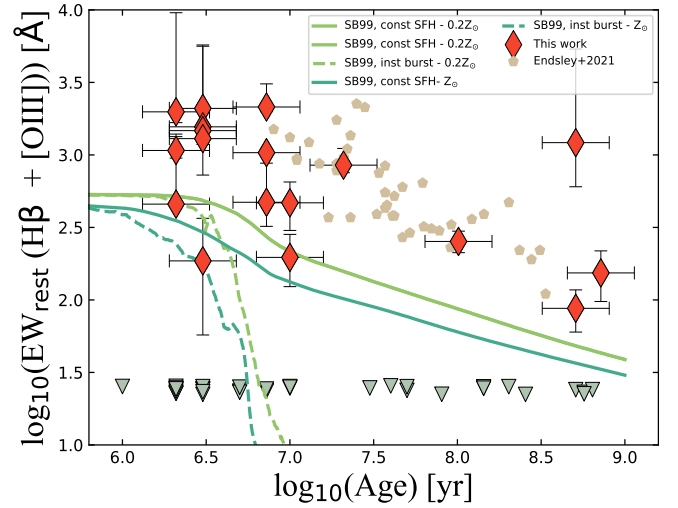


Figure 4. Age versus $(H\beta + [OIII])$ rest-frame EW. The gray triangles refer to the upper limits we estimated for all those galaxies we classified as non-emitters during our selection. We also report data points from Endsley et al. (2021) to make a comparison with the recent literature at high redshift. The curves refer to the evolution of the $H\beta$ rest-frame EW as a function of the age. We plot these tracks for the two metallicity (solar and sub-solar) we have considered in our work and for two different SFHs. A clear anti-correlation between rest-frame EW and age is evident in this plot, as found at lower redshifts from Reddy et al. (2018). The same has been found in Endsley et al. (2021) as well.

4.2. $H\alpha$ -derived SFR and the location of galaxies on the SFR- M_* plane

For all the 12 $H\alpha$ emitters at $z \simeq 7 - 8$ as determined from the MIRI $5.6 \mu\text{m}$ imaging, we estimated their star formation rate (SFR) from their inferred $H\alpha$ luminosities.

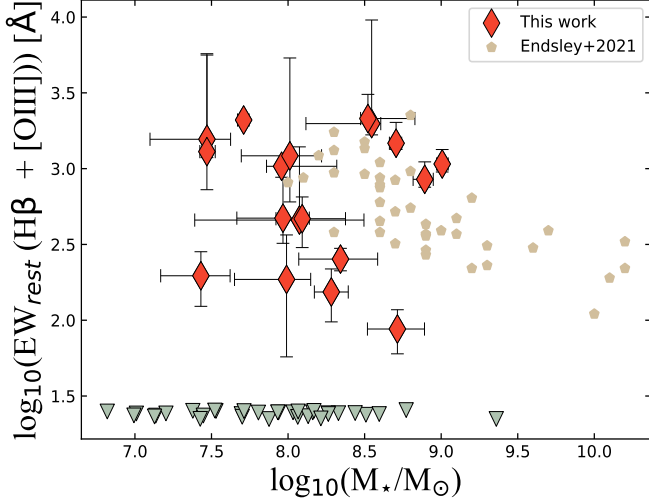


Figure 5. Stellar mass versus $(H\beta + [OIII])$ rest-frame EW. The gray triangles refer to the upper limits we estimated for all those galaxies we classified as non-emitters during our selection. Also in this case, we report data points from Endsley et al. (2021) to make a comparison with the recent literature at high redshift. The rest-frame EW broadly anti-correlates with stellar mass, similarly to what has been reported by Reddy et al. (2018) and Endsley et al. (2021) at lower redshifts.

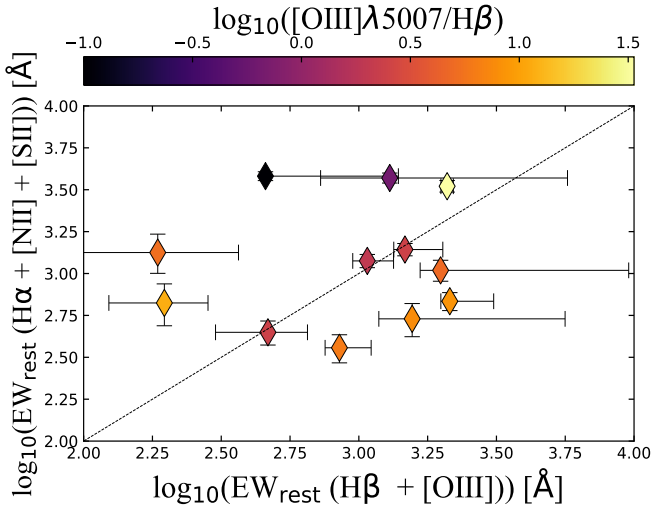


Figure 6. $(H\beta + [OIII])$ rest-frame EW versus $(H\alpha + [NII] + [SII])$ rest-frame EW. Here we colour-coded our data points for the $[OIII]\lambda 5007/H\beta$ flux ratio. There are some data points there are well above the identity line and show a $[OIII]\lambda 5007/H\beta$ which is dominated by $H\beta$. However, there are a few galaxies that lie above the identity line that show $[OIII]\lambda 5007/H\beta > 1$ which can be explained by a non-negligible dust extinction.

After we obtained the net observed $H\alpha$ flux for each source, we converted those fluxes into the intrinsic ones

by simply applying the Calzetti reddening law. We then estimate the luminosity for the $H\alpha$ emission line and apply the following formula from Kennicutt (1998) to obtain the corresponding $SFR(H\alpha)$:

$$SFR(M_{\odot} \text{ yr}^{-1}) = 7.9 \times 10^{-42} L_{H\alpha}(\text{erg s}^{-1}). \quad (2)$$

We then corrected this value following Madau & Dickinson (2014) to rescale it to a Chabrier IMF (Chabrier 2003) since Kennicutt’s formula has been calibrated for a Salpeter IMF (Salpeter 1955) over $(0.1 - 100) M_{\odot}$.

We then placed our sources on the $SFR - M_{\star}$ plane, as we show in Fig. 7. To make a comparison with the recent literature, we also populated this plane with star-forming galaxies at $z \simeq 3.0 - 6.5$ from Rinaldi et al. (2022) and $(H\beta + [OIII])$ emitters at $z \simeq 6.8 - 7$ (Endsley et al. 2021). We also indicate the starburst (SB) zone as determined in Caputi et al. (2017, 2021), who empirically defined as starburst galaxies all those sources with a specific SFR (sSFR) $> 10^{-7.60} \text{ yr}^{-1}$.

We see that 5 ($\simeq 42\%$) of the galaxies that show an “ $H\alpha$ excess” lie on the starburst zone, while only two are located on the star-formation main sequence (MS; Brinchmann et al. 2004; Noeske et al. 2007; Peng et al. 2010; Speagle et al. 2014; Rinaldi et al. 2022). The remaining 5 galaxies appear close, but slightly below the starburst envelope, in what has been defined in Caputi et al. (2017) as the star formation valley (SFV), i.e. in between the starburst cloud and the MS, suggesting that they are on the way to/from a starbursting phase. The fact that the vast majority of emitters are in or close the starburst zone is consistent with the findings of Endsley et al. (2021) for brighter galaxies, as it can be seen in Fig. 7.

We also colour-coded our $H\alpha$ emitters according to their $[OIII]\lambda 5007/H\beta$ ratios. We find no correlation between these ratios and the position of galaxies on the $SFR - M_{\star}$ plane.

4.3. The role of the $H\alpha$ emitters in the Cosmic Star Formation History at $z \simeq 7 - 8$

With the SFR values derived in the previous section, we computed the contribution of the prominent $H\alpha$ emitters to the cosmic Star Formation Rate Density (SFRD) at $z \simeq 7 - 8$. We estimated that, at these redshifts, $\log_{10}(\rho_{SFR_{H\alpha}}) \simeq -2.35$. In Fig. 8 we show the redshift evolution of the SFRD as proposed by Lilly et al. (1996); Madau et al. (1996), the so-called Lilly-Madau diagram. In this plot, we show our own estimation of the SFRD, along with a compilation of recent results from the literature based on different SFR tracers. In particular, we also show the SFRD values that have recently

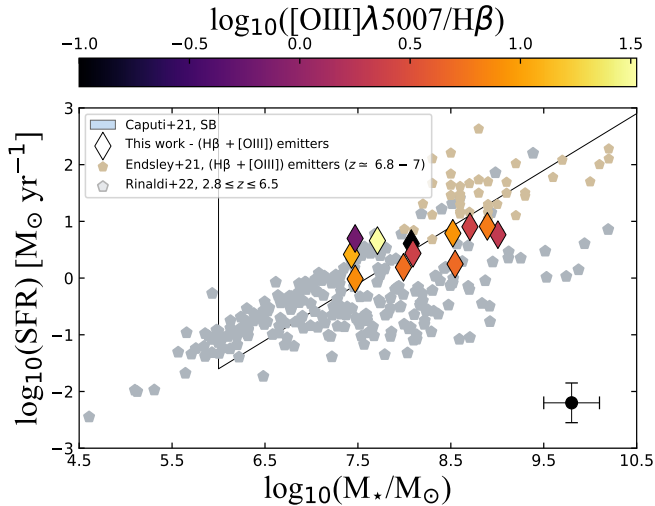


Figure 7. Stellar mass versus SFR. Here show the SFR– M_* plane populated by the SFR directly inferred from the $H\alpha$ excess. To make a comparison with the recent literature at high redshifts, we plot data points from Rinaldi et al. (2022) that gives us the opportunity to populate this plane with very low-mass galaxies at $z \simeq 2.8 - 6.5$. We also show data points from Endsley et al. (2021), who studied a sample of 20 bright ($H\beta + [\text{OIII}]$) emitters at $z \simeq 6.8 - 7$, and indicate the starburst zone, as defined by Caputi et al. (2017, 2021). Our data points are colour-coded by their $[\text{OIII}]/H\beta$ ratio. We see no correlation between this ratio and the position of sources on the SFR– M_* plane.

been obtained by Bouwens et al. (2022) using JWST data, tracing the SFR directly from the UV continuum emission at $z \simeq 9$ to $z \simeq 15$. Our inferred SFRD appears to be in good agreement with what has been found in the literature at similar redshifts. We also find a very good agreement with the predictions from theoretical models (e.g., IllustrisTNG; Springel et al. 2018). In particular, in Fig. 8 we also show the total SFRD, which has been estimated from both $H\alpha$ emitter and non-emitters at $z \simeq 7 - 8$. For the non-emitters, the SFR has been obtained from the rest-frame ultraviolet (UV) continuum luminosity at 2000 \AA and adopting the conversion formula from Kennicutt (1998).

4.4. The evolution of the rest-frame $EW(H\alpha)$ as a function of redshift

Finally, our derived values of the $H\alpha$ rest-frame EW allow us to extend the study of the redshift evolution of this parameter to $z \simeq 7 - 8$. In Fig. 9 we present our results along with the most recent determinations from the literature (for sources at $z \simeq 0.5 - 6$, Erb et al. 2006; Shim et al. 2011; Fumagalli et al. 2012; Stark et al. 2013; Sobral et al. 2014b; Mármol-Queralto et al. 2016; Smit et al. 2016; Reddy et al. 2018; Lam et al. 2019; Atek

et al. 2022; Boyett et al. 2022; Sun et al. 2022) and a stacking analysis measurement by (Stefanon et al. 2022) at $z \simeq 8$. These previous works made use of different methods and techniques to determine the $H\alpha$ EW, such as medium/high-resolution spectroscopy, low-resolution grism spectroscopy, and narrow-band and broad-band photometry combined with SED modelling, as we did in this paper. In particular, our sources represent a unique sample of strong emitters at $z \simeq 7 - 8$ that allows us to populate a virtually unexplored part of parameter space. Indeed, at those redshifts ($z \simeq 8$), only Stefanon et al. (2022) made an estimation of the average $H\alpha$ rest-frame EW, by median stacking 102 Lyman-break galaxies (LBG) in the $3.6\mu\text{m}$, $4.5\mu\text{m}$, $5.8\mu\text{m}$, and $8.0\mu\text{m}$ bands from the *Spitzer* Infrared Array Camera (IRAC).

We also incorporate in the analysis the empirical prescriptions from Fumagalli et al. (2012) and Faisst et al. (2016), who predict that the rest-frame $EW(H\alpha)$ should evolve differently below and above $z \simeq 2$. Particularly, at $z < 2$, the $EW(H\alpha)$ should evolve $\propto (1+z)^{1.8}$, while at $z > 2$ it should evolve as $\propto (1+z)^{1.3}$. Our data points are in good agreement with the stacking estimate obtained by Stefanon et al. (2022). Some of these values are well above the empirical median extrapolation at those redshifts, while others are consistent with it. The prominent line emitters that we analyse here constitute almost about a quarter of all the MIRI-detected galaxies at $z \simeq 7 - 8$. The remaining MIRI sources at those redshifts should lie below the extrapolation of the empirical determination. This very large variation in the $H\alpha$ rest EW at $z \simeq 7 - 8$ suggests that, even at these very high redshifts, galaxies may be at different stages of their evolution, as we discuss in the next section.

5. SUMMARY AND CONCLUSIONS

In this paper we have taken advantage of the publicly available medium and broad-band NIRC2 imaging in the XDF, combined with the deepest MIRI $5.6\mu\text{m}$ imaging existing in the same field, to search for prominent ($H\beta + [\text{OIII}]$) and $H\alpha$ emitters at $z \simeq 7 - 8$. This is the first time that the $H\alpha$ emission line can be detected and its flux measured in individual galaxies at such high redshifts. This has been possible thanks to the unprecedented sensitivity of JWST observations, particularly those conducted with MIRI, for which the sensitivity gain is of more than an order of magnitude with respect to previous instruments operating at similar wavelengths (Iani et al. 2022).

We found 18 galaxies which are robust candidates to be prominent ($H\beta + [\text{OIII}]$) emitters at $z \simeq 7 - 8$, as determined from their F430M and F444W flux excess. These 18 galaxies constitute $\simeq 31\%$ of all the galaxies

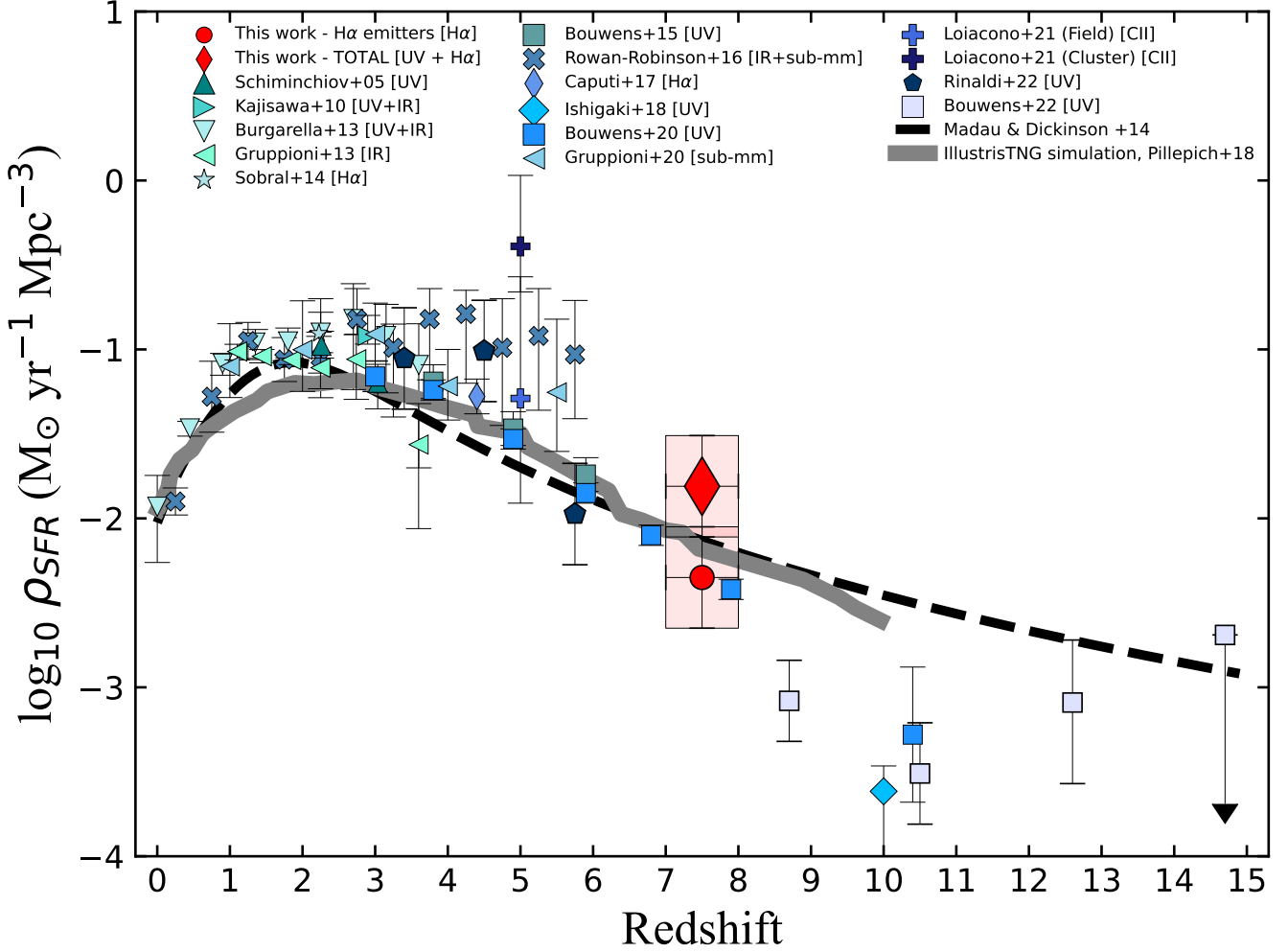


Figure 8. Cosmic star formation rate density as a function of the redshift. The large red circle indicates our estimate at $z \simeq 7 - 8$, which only takes into account the prominent $\text{H}\alpha$ emitters, i.e., it should be considered a lower limit to the real SFRD value at these redshifts. The red diamond, instead, refers to the total SFRD we estimated taking into account both the $\text{H}\alpha$ emitters and non-emitters at $z \simeq 7 - 8$. In particular, for the non-emitters, the SFR directly comes from the UV continuum emission. Other symbols refer to the recent SFRD determinations from the literature, based on different SFR tracers (Schiminovich et al. 2005; Kajisawa et al. 2010; Burgarella et al. 2013; Gruppioni et al. 2013; Sobral et al. 2014a; Bouwens et al. 2015; Rowan-Robinson et al. 2016; Caputi et al. 2017; Ishigaki et al. 2018; Bouwens et al. 2020; Gruppioni et al. 2020; Loiacono et al. 2021; Rinaldi et al. 2022; Bouwens et al. 2022). The different curves correspond to theoretical predictions. Dashed line: Madau & Dickinson (2014). Solid line: Pillepich et al. (2018). All the SFRD values in this figure correspond to a Chabrier (2003) IMF.

that we find in the XDF in the same redshift range. Among them, 16 lie on the MIRI coverage area and 12 out of 16 have a clear flux excess in the MIRI F560W filter, indicating the simultaneous presence of a prominent $\text{H}\alpha$ emission line. The $(\text{H}\beta + [\text{OIII}])$ rest-frame EWs that we derive range from $\simeq 87$ to 2140 \AA , with a median value of 943 \AA . For most of these galaxies, we find $[\text{OIII}]/\text{H}\beta > 1$, but a few have $[\text{OIII}]/\text{H}\beta < 1$. The two line fluxes can be separated making use of the independent $\text{H}\alpha$ emission line measurement. This is telling us that some of the prominent $(\text{H}\beta + [\text{OIII}])$ emitters

likely have hard radiation fields typical of low-metallicity galaxies, but not all of them. Some are strong line emitters simply because they are intensively forming stars.

The identified $\text{H}\alpha$ emitters show a rest-frame EW that ranges from a few hundred to a few thousand Angstroms. Some of these values are substantially above the expected median $\text{H}\alpha$ EW at these redshifts, as extrapolated from lower redshift determinations. We note, however, that the prominent $\text{H}\alpha$ emitters only constitute about a quarter of all the MIRI-detected galaxies at $z \simeq 7 - 8$. For the remaining galaxies, the rest-frame

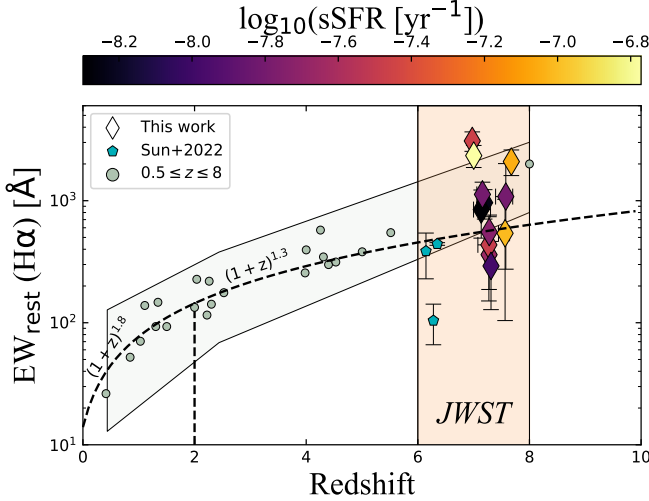


Figure 9. Evolution of the rest-frame $\text{EW}(\text{H}\alpha)$ as a function of the redshift. Our data points are colour-coded for sSFR . We also report the recent literature regarding the evolution of the rest-frame $\text{EW}(\text{H}\alpha)$ as a function of the redshift. The gray shade represents a median estimate of the error bars of the data points from the literature. The orange shade represents the redshift window where JWST is starting to detect these kind of sources more systematically (e.g., Boyett et al. 2022; Sun et al. 2022). Note that the data point at $z \simeq 8$, that comes from Stefanon et al. (2022), has been obtained by median stacking a sample of 102 Lyman-break galaxies in the *Spitzer*/IRAC bands from $3.6\mu\text{m}$ to $8\mu\text{m}$.

$\text{H}\alpha$ EW should lie below the expected median trend. As the $\text{H}\alpha$ EW is a good proxy for the sSFR , the lower EW values could indicate that these other galaxies (the non-emitters) have either relatively low star-formation rates, or a more important underlying stellar population producing a higher continuum. This is likely the case for the non-emitters at $z \simeq 7 - 8$ which are relatively evolved galaxies, with best-fit ages $> 10^7 - 10^8$ and stellar masses $> 10^8 M_\odot$.

In turn, most of the prominent ($\text{H}\beta + [\text{OIII}]$) and $\text{H}\alpha$ emitters are characterised by higher sSFR , with basically all of them being starburst galaxies or on the way to/from the starburst cloud. The majority of the prominent ($\text{H}\beta + [\text{OIII}]$) emitters are very young galaxies (best-fit ages $< 10^7$ yr), so they might be in their first major star-formation episode. A few others are almost as old as the Universe at their redshifts and have already built significant stellar mass ($> 10^8 M_\odot$), suggesting that they may be experiencing a rejuvenation effect.

Therefore, an overall conclusion of this work is that the galaxies present at the EoR are likely at different stages of their evolution. And strong line emission is present in a minor, but significant, fraction of sources.

Considering the $\text{H}\alpha$ fluxes inferred for the prominent $\text{H}\alpha$ emitters, we estimated their contribution to the cosmic SFRD at $z \simeq 7 - 8$. We obtained $\log_{10}(\rho_{\text{SFR}}) = -2.35 \pm 0.30$, in excellent agreement with independent measurements from the literature based on rest-frame UV luminosities, and with theoretical predictions and empirical extrapolations from lower redshifts. We note, however, that this estimated SFRD must be considered a lower limit, as it only takes into account the most prominent $\text{H}\alpha$ emitters at $z \simeq 7 - 8$. We also considered the SFR_{UV} for all the other galaxies at $z \simeq 7 - 8$ to obtain a total SFRD value at $z \simeq 7 - 8$. We concluded that the strong $\text{H}\alpha$ emitters produced about a third of the total SFRD at $z \simeq 7 - 8$, which suggests that they likely have had an important role in the process of reionization. In a future paper we will conduct a more detailed investigation of these sources, in order to better understand their nature.

The authors would like to thank Vasily Kokorev and Rafael Navarro-Carrera for technical help and useful discussions.

This work is based on observations made with the NASA/ESA/CSA James Webb Space Telescope. The data were obtained from the Mikulski Archive for Space Telescopes at the Space Telescope Science Institute, which is operated by the Association of Universities for Research in Astronomy, Inc., under NASA contract NAS 5-03127 for JWST. These observations are associated with programs GO #1963, GO #1895 and GTO #1283. The authors acknowledge the team led by coPIs C. Williams, M. Maseda and S. Tacchella, and PI P. Oesch, for developing their respective observing programs with a zero-exclusive-access period. Also based on observations made with the NASA/ESA Hubble Space Telescope obtained from the Space Telescope Science Institute, which is operated by the Association of Universities for Research in Astronomy, Inc., under NASA contract NAS 526555. The work presented here is the effort of the entire MIRI team and the enthusiasm within the MIRI partnership is a significant factor in its success. MIRI draws on the scientific and technical expertise of the following organisations: Ames Research Center, USA; Airbus Defence and Space, UK; CEA-Irfu, Saclay, France; Centre Spatial de Liège, Belgium; Consejo Superior de Investigaciones Científicas, Spain; Carl Zeiss Optronics, Germany; Chalmers University of Technology, Sweden; Danish Space Research Institute, Denmark; Dublin Institute for Advanced Studies, Ireland; European Space Agency, Netherlands; ETCA, Belgium; ETH Zurich, Switzerland; Goddard Space Flight Center, USA; Institut d'Astrophysique Spatiale, France; Instituto Na-

cional de Técnica Aeroespacial, Spain; Institute for Astronomy, Edinburgh, UK; Jet Propulsion Laboratory, USA; Laboratoire d'Astrophysique de Marseille (LAM), France; Leiden University, Netherlands; Lockheed Advanced Technology Center (USA); NOVA Opt-IR group at Dwingeloo, Netherlands; Northrop Grumman, USA; Max-Planck Institut für Astronomie (MPIA), Heidelberg, Germany; Laboratoire d'Etudes Spatiales et d'Instrumentation en Astrophysique (LESIA), France; Paul Scherrer Institut, Switzerland; Raytheon Vision Systems, USA; RUAG Aerospace, Switzerland; Rutherford Appleton Laboratory (RAL Space), UK; Space Telescope Science Institute, USA; Toegestap- Natuurwetenschappelijk Onderzoek (TNO-TPD), Netherlands; UK Astronomy Technology Centre, UK; University College London, UK; University of Amsterdam, Netherlands; University of Arizona, USA; University of Cardiff, UK; University of Cologne, Germany; University of Ghent; University of Groningen, Netherlands; University of Leicester, UK; University of Leuven, Belgium; University of Stockholm, Sweden; Utah State University, USA

KIC and EI acknowledge funding from the Netherlands Research School for Astronomy (NOVA). KIC acknowledges funding from the Dutch Research Council (NWO) through the award of the Vici Grant VI.C.212.036. The Cosmic Dawn Center is funded by the Danish National Research Foundation under

grant No. 140. LC acknowledges financial support from Comunidad de Madrid under Atracción de Talento grant 2018-T2/TIC-11612. SG acknowledges the support of the Cosmic Dawn Center of Excellence funded by the Danish National Research Foundation under grant 140. G.Ö., A.B. & J.M. acknowledge support from the Swedish National Space Administration (SNSA). AAH acknowledges support from PID2021-124665NB-I00 funded by the Spanish Ministry of Science and Innovation and the State Agency of Research MCIN/AEI/10.13039/501100011033. J.H. and D.L. were supported by a VILLUM FONDEN Investigator grant to J.H. (project number 16599).

JAM acknowledge support by grant PIB2021-127718NB-100 by the Spanish Ministry of Science and Innovation/State Agency of Research MCIN/AEI/ 10.13039/501100011033 and by ERDF A way of making Europe.

Facilities: *HST*, *JWST*.

Software: *Astropy* (Astropy Collaboration et al. 2018), *LePHARE* (Arnouts & Ilbert 2011), *NumPy* (Harris et al. 2020), *pandas* (pandas development team 2020) *Photutils* (Bradley et al. 2021), *SciPy* (Virtanen et al. 2020) *Source Extractor* (Bertin & Arnouts 1996), *TOPCAT* (Taylor 2005).

REFERENCES

- Anders, P., & Fritze-v. Alvensleben, U. 2003, *A&A*, 401, 1063
- Arellano-Córdova, K. Z., Berg, D. A., Chisholm, J., et al. 2022, *ApJL*, 940, L23
- Arnouts, S., & Ilbert, O. 2011, *LePHARE: Photometric Analysis for Redshift Estimate*, , ascl:1108.009
- Astropy Collaboration, Price-Whelan, A. M., Sipőcz, B. M., et al. 2018, *AJ*, 156, 123
- Atek, H., Furtak, L., Oesch, P., et al. 2022, *arXiv e-prints*, arXiv:2202.04081
- Babusiaux, C., Fabricius, C., Khanna, S., et al. 2022, *arXiv e-prints*, arXiv:2206.05989
- Bagley, M. B., Finkelstein, S. L., Koekemoer, A. M., et al. 2022, *arXiv e-prints*, arXiv:2211.02495
- Bertin, E., & Arnouts, S. 1996, *A&AS*, 117, 393
- Bouwens, R., González-López, J., Aravena, M., et al. 2020, *ApJ*, 902, 112
- Bouwens, R. J., Illingworth, G. D., Oesch, P. A., et al. 2015, *ApJ*, 803, 34
- Bouwens, R. J., Stefanon, M., Brammer, G., et al. 2022, *arXiv e-prints*, arXiv:2211.02607
- Boyet, K., Mascia, S., Pentericci, L., et al. 2022, *ApJL*, 940, L52
- Bradley, L., Sipőcz, B., Robitaille, T., et al. 2021, *astropy/photutils*: 1.0.2, v1.0.2, Zenodo, doi:10.5281/zenodo.4453725
- Brinchmann, J., Charlot, S., White, S. D. M., et al. 2004, *MNRAS*, 351, 1151
- Bruzual, G., & Charlot, S. 2003, *MNRAS*, 344, 1000
- Burgarella, D., Buat, V., Gruppioni, C., et al. 2013, *A&A*, 554, A70
- Calzetti, D., Armus, L., Bohlin, R. C., et al. 2000, *ApJ*, 533, 682
- Caputi, K. I., Cirasuolo, M., Dunlop, J. S., et al. 2011, *MNRAS*, 413, 162
- Caputi, K. I., Deshmukh, S., Ashby, M. L. N., et al. 2017, *ApJ*, 849, 45
- Caputi, K. I., Caminha, G. B., Fujimoto, S., et al. 2021, *ApJ*, 908, 146
- Caruana, J., Bunker, A. J., Wilkins, S. M., et al. 2014, *MNRAS*, 443, 2831
- Chabrier, G. 2003, *PASP*, 115, 763

- De Barros, S., Oesch, P. A., Labbé, I., et al. 2019, *MNRAS*, 489, 2355
- Endsley, R., Stark, D. P., Chevallard, J., & Charlot, S. 2021, *MNRAS*, 500, 5229
- Erb, D. K., Steidel, C. C., Shapley, A. E., et al. 2006, *ApJ*, 647, 128
- Faisst, A. L., Capak, P., Hsieh, B. C., et al. 2016, *ApJ*, 821, 122
- Fontana, A., Vanzella, E., Pentericci, L., et al. 2010, *ApJL*, 725, L205
- Fumagalli, M., Patel, S. G., Franx, M., et al. 2012, *ApJL*, 757, L22
- Galametz, A., Grazian, A., Fontana, A., et al. 2013, *ApJS*, 206, 10
- Gruppioni, C., Pozzi, F., Rodighiero, G., et al. 2013, *MNRAS*, 436, 2875
- Gruppioni, C., Béthermin, M., Loiacono, F., et al. 2020, *A&A*, 643, A8
- Harris, C. R., Millman, K. J., van der Walt, S. J., et al. 2020, *Nature*, 585, 357.
<https://doi.org/10.1038/s41586-020-2649-2>
- Iani, E., Caputi, K. I., Rinaldi, P., & Kokorev, V. I. 2022, *ApJL*, 940, L24
- Illingworth, G. D., Magee, D., Oesch, P. A., et al. 2013, *ApJS*, 209, 6
- Ishigaki, M., Kawamata, R., Ouchi, M., et al. 2018, *ApJ*, 854, 73
- Kajisawa, M., Ichikawa, T., Yamada, T., et al. 2010, *ApJ*, 723, 129
- Kennicutt, Robert C., J. 1998, *ARA&A*, 36, 189
- Khostovan, A. A., Sobral, D., Mobasher, B., et al. 2016, *MNRAS*, 463, 2363
- Kron, R. G. 1980, *ApJS*, 43, 305
- Labbé, I., Oesch, P. A., Bouwens, R. J., et al. 2013, *ApJL*, 777, L19
- Lam, D., Bouwens, R. J., Labbé, I., et al. 2019, *A&A*, 627, A164
- Leitherer, C., Schaerer, D., Goldader, J. D., et al. 1999, *ApJS*, 123, 3
- Lilly, S. J., Le Fevre, O., Hammer, F., & Crampton, D. 1996, *ApJL*, 460, L1
- Loiacono, F., Decarli, R., Gruppioni, C., et al. 2021, *A&A*, 646, A76
- Madau, P., & Dickinson, M. 2014, *ARA&A*, 52, 415
- Madau, P., Ferguson, H. C., Dickinson, M. E., et al. 1996, *MNRAS*, 283, 1388
- Mármol-Queraltó, E., McLure, R. J., Cullen, F., et al. 2016, *MNRAS*, 460, 3587
- Matthee, J., Mackenzie, R., Simcoe, R. A., et al. 2022, arXiv e-prints, arXiv:2211.08255
- Morishita, T., & Stiavelli, M. 2022, arXiv e-prints, arXiv:2207.11671
- Noeske, K. G., Weiner, B. J., Faber, S. M., et al. 2007, *ApJL*, 660, L43
- Oesch, P., Bouwens, R., Brammer, G., et al. 2021, FRESCO: The First Reionization Epoch Spectroscopic Complete Survey, JWST Proposal. Cycle 1, ID. #1895, ,
- Oke, J. B., & Gunn, J. E. 1983, *ApJ*, 266, 713
- Ono, Y., Ouchi, M., Mobasher, B., et al. 2012, *ApJ*, 744, 83
- Osterbrock, D. E., & Ferland, G. J. 2006, *Astrophysics of gaseous nebulae and active galactic nuclei*
- Ostlin, G., Luis, C., & Collaborators., C. K. 2023, in prep.
- pandas development team, T. 2020, pandas-dev/pandas: Pandas, vlatest, Zenodo, doi:10.5281/zenodo.3509134.
<https://doi.org/10.5281/zenodo.3509134>
- Peng, Y.-j., Lilly, S. J., Kovač, K., et al. 2010, *ApJ*, 721, 193
- Pentericci, L., Vanzella, E., Fontana, A., et al. 2014, *ApJ*, 793, 113
- Pillepich, A., Springel, V., Nelson, D., et al. 2018, *MNRAS*, 473, 4077
- Reddy, N. A., Shapley, A. E., Sanders, R. L., et al. 2018, *ApJ*, 869, 92
- Rieke, G. H., Wright, G. S., Böker, T., et al. 2015, *PASP*, 127, 584
- Rieke, M. J., Kelly, D., & Horner, S. 2005, in *Society of Photo-Optical Instrumentation Engineers (SPIE) Conference Series*, Vol. 5904, *Cryogenic Optical Systems and Instruments XI*, ed. J. B. Heaney & L. G. Burriesci, 1–8
- Rinaldi, P., Caputi, K. I., van Mierlo, S. E., et al. 2022, *ApJ*, 930, 128
- Roberts-Borsani, G. W., Bouwens, R. J., Oesch, P. A., et al. 2016, *ApJ*, 823, 143
- Rosani, G., Caminha, G. B., Caputi, K. I., & Deshmukh, S. 2020, *A&A*, 633, A159
- Rowan-Robinson, M., Oliver, S., Wang, L., et al. 2016, *MNRAS*, 461, 1100
- Salpeter, E. E. 1955, *ApJ*, 121, 161
- Schaerer, D., & de Barros, S. 2009, *A&A*, 502, 423
- Schiminovich, D., Ilbert, O., Arnouts, S., et al. 2005, *ApJL*, 619, L47
- Schlaafly, E. F., & Finkbeiner, D. P. 2011, *ApJ*, 737, 103
- Shim, H., Chary, R.-R., Dickinson, M., et al. 2011, *ApJ*, 738, 69
- Smit, R., Bouwens, R. J., Labbé, I., et al. 2016, *ApJ*, 833, 254
- Sobral, D., Best, P. N., Smail, I., et al. 2014a, *MNRAS*, 437, 3516
- . 2014b, *MNRAS*, 437, 3516

- Sonnnett, S., Meech, K., Jedicke, R., et al. 2013, *PASP*, 125, 456
- Speagle, J. S., Steinhardt, C. L., Capak, P. L., & Silverman, J. D. 2014, *ApJS*, 214, 15
- Springel, V., Pakmor, R., Pillepich, A., et al. 2018, *MNRAS*, 475, 676
- Stark, D. P., Schenker, M. A., Ellis, R., et al. 2013, *ApJ*, 763, 129
- Stark, D. P., Richard, J., Charlot, S., et al. 2015, *MNRAS*, 450, 1846
- Stasińska, G., & Leitherer, C. 1996, *ApJS*, 107, 661
- Stefanon, M., Bouwens, R. J., Illingworth, G. D., et al. 2022, *ApJ*, 935, 94
- Sun, F., Egami, E., Pirzkal, N., et al. 2022, arXiv e-prints, arXiv:2209.03374
- Tang, M., Stark, D. P., Chevallard, J., & Charlot, S. 2019, *MNRAS*, 489, 2572
- Taylor, M. B. 2005, in *Astronomical Society of the Pacific Conference Series*, Vol. 347, *Astronomical Data Analysis Software and Systems XIV*, ed. P. Shopbell, M. Britton, & R. Ebert, 29
- Trump, J. R., Arrabal Haro, P., Simons, R. C., et al. 2022, arXiv e-prints, arXiv:2207.12388
- Virtanen, P., Gommers, R., Oliphant, T. E., et al. 2020, *Nature Methods*, 17, 261
- Wang, X., Cheng, C., Ge, J., et al. 2022, arXiv e-prints, arXiv:2212.04476
- Whitaker, K. E., Ashas, M., Illingworth, G., et al. 2019, *ApJS*, 244, 16
- Williams, C. C., Maseda, M., Tacchella, S., et al. 2021, UDF medium band survey: Using H-alpha emission to reconstruct Ly-alpha escape during the Epoch of Reionization, JWST Proposal. Cycle 1, ID. #1963, ,
- Wright, G. S., Wright, D., Goodson, G. B., et al. 2015, *PASP*, 127, 595